

ON SHOCKS DRIVEN BY HIGH-MASS PLANETS IN RADIATIVELY INEFFICIENT DISKS. I. TWO-DIMENSIONAL GLOBAL DISK SIMULATIONS

ALEXANDER J.W. RICHERT^{1,2,3,4}, WLADIMIR LYRA^{3,4,5}, AARON BOLEY⁶
MORDECAI-MARK MAC LOW⁷ & NEAL TURNER³

Draft version October 28, 2018

ABSTRACT

Recent observations of gaps and non-axisymmetric features in the dust distributions of transition disks have been interpreted as evidence of embedded massive protoplanets. However, comparing the predictions of planet-disk interaction models to the observed features has shown far from perfect agreement. This may be due to the strong approximations used for the predictions. For example, spiral arm fitting typically uses results that are based on low-mass planets in an isothermal gas. In this work, we describe two-dimensional, global, hydrodynamical simulations of disks with embedded protoplanets, with and without the assumption of local isothermality, for a range of planet-to-star mass ratios 1–10 M_J for a 1 M_\odot star. We use the PENCIL CODE in polar coordinates for our models. We find that the inner and outer spiral wakes of massive protoplanets ($M \gtrsim 5 M_J$) produce significant shock heating that can trigger buoyant instabilities. These drive sustained turbulence throughout the disk when they occur. The strength of this effect depends strongly on the mass of the planet and the thermal relaxation timescale; for a 10 M_J planet embedded in a thin, purely adiabatic disk, the spirals, gaps, and vortices typically associated with planet-disk interactions are disrupted. We find that the effect is only weakly dependent on the initial radial temperature profile. The spirals that form in disks heated by the effects we have described may fit the spiral structures observed in transition disks better than the spirals predicted by linear isothermal theory.

Subject headings: hydrodynamics — planet-disk interactions — planets and satellites: formation — protoplanetary disks — shock waves — turbulence

1. INTRODUCTION

Decades of analytical and numerical work (Papaloizou & Lin 1984; Lin & Papaloizou 1986a,b; Nelson et al. 2000; Masset & Snellgrove 2001; Paardekoope & Mellema 2004; Quillen et al. 2004; de Val-Borro et al. 2006; Klahr & Kley 2006; Lyra et al. 2009; Zhu et al. 2011; Kley et al. 2012; Kley & Nelson 2012) have established that massive ($\gtrsim 1 M_J$) protoplanets generate observable gaps and other features in their host disks that can in principle be resolved by ALMA (see, e.g., the review of Wolf et al. 2012). These models show that the gravitationally-induced tides of protoplanets with masses exceeding Saturn’s clear axisymmetric gaps in the disk. These generate long-lived, non-axisymmetric vortices due to the Rossby wave instability (RWI) at the

gap edges (Lovelace & Hohlfield 1978; Toomre 1981; Papaloizou & Pringle 1984, 1985; Hawley 1987; Lovelace et al. 1999). Non-axisymmetric dust clouds have been observed in transition disks at sub-mm wavelengths (Oppenheimer et al. 2008; Brown et al. 2009; Casassus et al. 2012; Isella et al. 2013; Casassus et al. 2013; van der Marel et al. 2013), features that are usually interpreted as vortices induced by embedded protoplanets. Spiral structures, one of the hallmarks of planet-disk interactions (Goldreich & Tremaine 1979, Ogilvie & Lubow 2002, Rafikov 2002), are also seen in several transition disks in polarized scattered light (Muto et al. 2012, Garufi et al. 2013, Avenhaus et al. 2014, Currie et al. 2014).

However, because the putative corresponding planets are not directly observed, sufficiently detailed dynamical and radiative transfer models must be consistent with observations, and all other possible ways to produce the observed features must be ruled out. For example, there are several mechanisms that are known to generate vortices without a planet in the disk. The RWI can occur at dead zone boundaries (Varnière & Tagger 2006; Lyra et al. 2008), whether at the inner edge of the dead zone (Lyra & Mac Low 2012), or at the outer one (Lyra et al. 2015), despite the transition in resistivity in the outer disk being smooth (Dzyurkevich et al. 2013). In regions without the steep vortensity gradient required for the RWI, a vortex could be maintained by baroclinic feedback as long as (1) a non-zero entropy gradient exists (Klahr & Bodenheimer 2003; Klahr 2004), (2) the thermal time is finite (Petersen et al. 2007a,b; Lesur & Papaloizou 2010; Raettig et al. 2013), and (3)

¹ Department of Astronomy & Astrophysics, Penn State University, 525 Davey Lab, University Park, PA 16802, USA. ajr327@psu.edu

² Center for Exoplanets & Habitable Worlds, Pennsylvania State University.

³ Jet Propulsion Laboratory, California Institute of Technology, 4800 Oak Grove Drive, Pasadena, CA, 91109, USA. wlyra@jpl.nasa.gov, neal.j.turner@jpl.nasa.gov

⁴ Division of Geological & Planetary Sciences, California Institute of Technology, 1200 E California Blvd MC 150-21, Pasadena, CA 91125 USA

⁵ Sagan Fellow

⁶ Department of Physics and Astronomy, University of British Columbia, 6224 Agricultural Road, Vancouver, BC V6T 1Z1, Canada. acoley@phas.ubc.ca

⁷ Department of Astrophysics, American Museum of Natural History, Central Park West at 79th Street, New York, NY 10024-5192, USA. mordecai@amnh.org

magnetization is absent (Lyra & Klahr 2011). Such conditions may or may not occur in the outer regions of protoplanetary disks.

There are also difficulties in interpreting gaps as unambiguous signposts of planet-disk interactions. The transition disk surrounding HD 100546, for instance, contains a gap, but the gap edge is far too smooth to have been caused by a planet (Mulders et al. 2013). In optically thin disks, Lyra & Kuchner (2013) find that the combination of photoelectric heating and dust trapping can lead to the production of sharp rings similar to those commonly attributed to gravitational shepherding by planets. Furthermore, the magnetorotational instability (MRI; Balbus & Hawley 1991) could lead to gaps in the dust distribution by inducing zonal flows that are triggered by magnetic flux accumulation in turbulence (Lyra et al. 2008; Johansen et al. 2009; Simon et al. 2012; Kunz & Lesur 2013; Flock et al. 2015).

Finally, a one-to-one correlation between planets and spirals is also absent. Shear causes any density wave in a differentially rotating disk to propagate as a spiral. Therefore, the observed spiral features could easily be the result of disk turbulence. For example, Lyra et al. (2015) show that waves from the MRI-active zone propagate into the MRI-dead zone as a coherent spiral. In fact, it has been difficult to explain the spiral features observed in transition disk as unequivocally due to planets. The observed spirals have, in general, very large pitch angles, which is inconsistent with the background disk temperature if linear spiral density wave theory for an isothermal gas is assumed (Rafikov 2002; Muto et al. 2012). Currie et al. (2014) present a remarkable spiral feature in the disk around HD 100546, with little polarization, that can only be fit with an effective disk temperature of ≈ 1000 K, substantially higher than the expected gas temperatures. Benisty et al. (2015) show that fitting a model to the spiral in the disk around MWC 758 requires a large disk aspect ratio around the spiral features, corresponding to 300 K at 55 AU, whereas the background gas is at much colder temperatures, 50 K. Juhasz et al. (2014) show that a local increase in pressure scale height by at least 20% would be required to reproduce observations of multiple disks in polarized scattered light.

The high temperatures implied by these spiral features motivate us to abandon the idea of local isothermality, and instead to entertain potential effects due to the departure from barotropic conditions. Although numerical simulations of planet-disk interactions have been performed for decades, a search of the literature reveals that most previous works have either made use of the locally isothermal approximation or examined planetary masses of no more than $\sim 1\text{--}5 M_J$. As some of the candidate planets in transition disks are very massive ($\geq 10 M_J$), we also examine that region of the parameter space. We find that the wake generated by the most massive planets has relative Mach numbers above unity compared to the quiescent disk. The resulting shocks heat the surrounding gas, effectively converting the planet's gravitational potential energy into a powerful extra energy source for disk heating. For cases with sufficiently long cooling times (and in which the thin-disk approximation holds), a radial buoyant instability

occurs, leading to turbulence around the planet and disruption of the usual wake features, i.e., spirals, gaps, and vortices.

This paper is the first in a series in which we compare the behavior of planets embedded in disks that are evolved with and without the assumption of local isothermality. The next paper in the series will extend the two-dimensional (2D) study presented here to include three-dimensional disks. In Sect. 2, we present our numerical model. We discuss the simulation results in Sect. 3, and conclude in Sect. 4.

2. THE MODEL

2.1. Governing equations

In this work, we perform two-dimensional global hydrodynamical simulations of gas disks with an embedded massive planet to explore the effects of shocks that result from planet-disk interactions in non-barotropic disks. We primarily use the PENCIL CODE⁸, a high-order finite-difference grid hydrodynamics code. An independent code, BOXZYHYDRO, is also used to validate the main results, as described in Sect. 3.3. For the Pencil simulations, the gas density is evolved using the continuity equation

$$\frac{D\Sigma}{Dt} = -\Sigma \nabla \cdot \mathbf{u} \quad (1)$$

and the equation of motion

$$\frac{D\mathbf{u}}{Dt} = -\frac{1}{\Sigma} \nabla P - \nabla \Phi + \frac{1}{\Sigma} \nabla \cdot \boldsymbol{\zeta}, \quad (2)$$

where Σ , \mathbf{u} , and P are the surface density, velocity, and pressure of the gas, respectively, and Φ represents the gravitational potential contributions of the star and planet (we have ignored the effects of gas self-gravity). The operator

$$\frac{D}{Dt} \equiv \frac{\partial}{\partial t} + \mathbf{u} \cdot \nabla \quad (3)$$

represents the advective derivative. The last term in the equation of motion is the acceleration due to shock viscosity. Assuming that the shock viscosity ν_{sh} takes the form of a bulk viscosity, the stress tensor is

$$\boldsymbol{\zeta}_{ij} = \nu_{\text{sh}} \Sigma \delta_{ij} \nabla \cdot \mathbf{u}, \quad (4)$$

The shock viscosity must be a localized function, ensuring that sufficient energy is dissipated in regions of the flow where shocks occur to satisfy the Rankine-Hugoniot jump conditions, while more quiescent regions are left unaffected. We take

$$\nu_{\text{sh}} = c_{\text{sh}} \left\langle \max\left[\frac{(-\nabla \cdot \mathbf{u})_+}{3}\right] \right\rangle [\min(\Delta r, r\Delta\phi)]^2. \quad (5)$$

The viscosity is proportional to the maximum of positive flow convergence, as evaluated over three grid cells in each direction for a total of 9 zones in 2D (the given cell plus its immediate neighbors). The angled brackets

⁸ See <http://pencil-code.googlecode.com>

represent a quadratic smoothing function that smooths the divergence over seven zones in each direction, with weights $(1, 6, 15, 20, 15, 6, 1)/64$. The result is then scaled by the square of the smallest grid spacing. In the above equation, r is the cylindrical radius and ϕ the azimuthal angle; Δr and $\Delta\phi$ give the numerical grid spacing. The quantity c_{sh} is a constant defining the strength of the shock viscosity, set to unity in our simulations. Varying this coefficient changes the area over which the added entropy is distributed but not the total amount of extra energy, which still must satisfy the jump conditions. We refer to c_{sh} as the shock viscosity coefficient (for more details see Haugen et al. 2004).

To follow the thermodynamic evolution of the disk, we assume the ideal gas law as the equation of state

$$P = \Sigma c_s^2 / \gamma, \quad (6)$$

where c_s is the adiabatic sound speed and γ is the adiabatic index. The temperature and sound speed are related according to

$$T = c_s^2 / [c_p(\gamma - 1)], \quad (7)$$

where $c_p = \gamma c_v$ is the specific heat at constant pressure, and c_v the specific heat at constant volume. They are related to the universal gas constant R by

$$R/\mu = c_p - c_v,$$

where μ is the mean molecular weight of the gas.

The Pencil Code implements thermodynamic evolution by solving for the entropy $S = c_v (\ln P - \gamma \ln \Sigma)$. We use thermal relaxation for non-isothermal runs, driving the temperature to a reference temperature T_{ref} within a time τ , according to

$$T \frac{DS}{Dt} = -c_v \frac{(T - T_{\text{ref}})}{\tau} + \Gamma_{\text{sh}}, \quad (8)$$

where both T_{ref} and τ are radially-varying. We take T_{ref} to be the initial temperature and τ proportional to the orbital period

$$\tau = \tau_0 \Omega_0 / \Omega, \quad (9)$$

where $\Omega = \sqrt{GM_*/r^3}$ is the Keplerian angular frequency. The subscript “0” refers to the values of the quantities at an arbitrary reference radius $r_0 = 1$. The reference timescale for thermal relaxation, τ_0 , is a free parameter of the model reflecting the radiative cooling timescale of the gas. The function

$$\Gamma_{\text{sh}} = \nu_{\text{sh}} (\nabla \cdot \mathbf{u})^2 \quad (10)$$

is the heating due to dissipation of shocks.

Sixth-order hyper-dissipation terms are added to the evolution equations to provide extra dissipation near the grid scale, as discussed in Lyra et al. (2008). These terms are needed for numerical stability because the high-order scheme of the Pencil Code formally lacks error terms to produce stabilizing numerical dissipation (McNally et al. 2012).

The simulations are run in the inertial frame, centered at the barycenter of the system. The positions of the star

and planet are evolved on circular orbits by direct integration using an N -body routine, employing the same 3rd-order Runge-Kutta algorithm used for updating the gas grid. Since we are modeling disks with high-mass protoplanets, this will allow us to capture any dynamical effects on the gas induced by stellar wobble. The gravitational potential Φ acting on the star, planet, and gas is the sum of the potential contributions of the star and planet (i.e. the gravity of the gas is ignored):

$$\Phi = - \sum_i^N \frac{GM_i}{\sqrt{\mathcal{R}_i^2 + b_i^2}}, \quad (11)$$

where $N = 2$, M_i is the mass of particle i , $\mathcal{R}_i = |r - r_i|$ is the distance between the i th particle and a gas parcel or massive particle for which the potential is being calculated, and b_i is the smoothing radius of the i th particle, which is used to prevent singularities. The gravitational smoothing radius of the planet is set to its Hill radius. The star does not require a smoothing radius because it lies outside the gas grid.

For units, the planetary semi-major axis and orbital velocity are used as the units of length and velocity, respectively. This in turn implies 2π time units per orbit.

2.2. Run parameters

All simulations are performed on a cylindrical grid with $(N_r, N_\theta) = (768, 1024)$, with $0.4 < r < 12$ (in units of the planet’s semi-major axis). Grid points are spaced in r according to a power law such that $\Delta r \propto r^{0.5}$, providing higher resolution in the vicinity of the planet compared with the outer disk (for our choice of initial temperature gradient, this non-equidistant grid corresponds to a constant number of radial grid cells per scale height). For all simulations, the initial density distribution is axisymmetric and decreases with the square root of the radius, with $\Sigma_0 = 1$ (the physical units of surface density can be chosen arbitrarily since the self-gravity of the gas has not been included). The sound speed at the reference radius was set to 5×10^{-2} , which corresponds to a temperature of ~ 100 K, assuming a $1 M_\odot$ star with planetary semi-major axis 5.2 AU, $\gamma = 7/5$, and mean molecular weight 2.4 (corresponding to a 5:2 hydrogen/helium mixture by mass). The initial sound speed is set to

$$c_s^2 = c_{s0}^2 r^\beta. \quad (12)$$

In order to study the role of thermodynamical evolution in disks containing high-mass protoplanets, we perform four sets of simulations. First, we perform simulations for three planet-to-star mass ratios $q = 10^{-3}$, 5×10^{-3} , and 10^{-2} , with locally isothermal and adiabatic disks. We run one adiabatic simulation with shock heating artificially turned off in the entropy equation ($\Gamma_{\text{sh}} = 0$), while keeping the acceleration due to shock viscosity turned on in the momentum equation. This is done to determine the role of shock heating in the non-barotropic simulations. For this test case, $q = 10^{-2}$. Next, we run three simulations with different values of the reference thermal relaxation timescale τ_0 , also with $q = 10^{-2}$. Finally, we run three additional simulations with mass ratio 10^{-2} , but using different radial power

TABLE 1
SIMULATION PARAMETERS

Run	q	β	γ	τ_0	Shock heating
Mass, thermal evolution; Figs. 1–4					
A	10^{-3}	-1	1	0	—
B	5×10^{-3}	-1	1	0	—
C	10^{-2}	-1	1	0	—
D	10^{-3}	-1	1.4	∞	Yes
E	5×10^{-3}	-1	1.4	∞	Yes
F	10^{-2}	-1	1.4	∞	Yes
Viscous heating; Fig. 3					
G	10^{-2}	-1	1.4	∞	No
Relaxation time; Fig. 5					
H	10^{-2}	-1	1.4	0.1	Yes
I	10^{-2}	-1	1.4	1	Yes
J	10^{-2}	-1	1.4	10	Yes
Temperature power law; Fig. 6					
K	10^{-2}	-0.5	1.4	∞	Yes
L	10^{-2}	-0.2	1.4	∞	Yes
M	10^{-2}	0	1.4	∞	Yes

laws for the initial temperature (all adiabatic). Table 1 contains run parameters for all simulations, thirteen in total, where q is the planet-to-star mass ratio, β is the slope of the radial temperature power law, γ is the adiabatic index of the gas, and τ_0 is the cooling timescale in units of orbits at the reference radius. Locally isothermal runs are denoted by $\tau_0 = 0$ and $\gamma = 1$, while adiabatic runs are denoted by $\tau_0 = \infty$. All simulations are run for 100 planetary orbits.

3. RESULTS

3.1. Global disk properties

3.1.1. Planet mass and thermal evolution

Fig. 1 shows the surface densities in the inner disk ($r < 4$) after 100 orbits for the locally isothermal ($\tau_0 = 0$) and adiabatic ($\tau_0 = \infty$) runs and for three values of the planet-star mass ratio q . For all q , there is a clear difference between the global morphologies of the isothermal and adiabatic disks. All three isothermal simulations show well-behaved spiral structure, a clear gap, and an accompanying vortex, as expected. In contrast, large-scale turbulence is clearly present in the $q = 5 \times 10^{-3}$ and 10^{-2} adiabatic runs, in which the expected gaps and vortices appear to be completely missing. For the $q = 10^{-3}$ adiabatic run, the presence of global turbulence is not as apparent, but the gap depth and the accompanying vortex are visibly diminished.

Since the turbulence seen in Fig. 1 is present only in runs with non-barotropic equation of state, we hypothesize that it is the result of buoyant oscillations triggered by hot gas that has been tidally compressed by the planet.

To test this hypothesis and confirm the originating region of any such oscillations, we compare the results of each simulation to the Solberg-Høiland stability criterion. The criterion for hydrodynamic stability is given by

$$\kappa^2 + N^2 \geq 0, \quad (13)$$

where the epicyclic frequency

$$\kappa \equiv \left[\frac{1}{r^3} \frac{d}{dr} (r^4 \dot{\theta}^2) \right]^{1/2}, \quad (14)$$

and the characteristic frequency of buoyant oscillations, the Brunt-Väisälä frequency,

$$N \equiv \left[\frac{1}{\Sigma} \frac{dP}{dr} \left(\frac{1}{\Sigma} \frac{d\Sigma}{dr} - \frac{1}{\gamma P} \frac{dP}{dr} \right) \right]^{1/2}. \quad (15)$$

In the case of a steep entropy gradient, N^2 will become negative, leading to buoyant instability. For positive κ^2 , the velocity shear of the disk will tend to damp buoyant oscillations. We calculate Λ for each simulation at several timesteps, where

$$\Lambda \equiv 1 + \frac{N^2}{\kappa^2} \quad (16)$$

is the left-hand side of Equation (13), normalized by κ^2 . For $\Lambda < 0$, the local shear of the disk will not stabilize buoyant oscillations. If the turbulence observed in Fig. 1 is due to buoyant instabilities, then Λ will achieve negative values only in the adiabatic simulations. This is because in the locally isothermal simulations neither the temperature profile (which remains constant through the simulation) nor the density fluctuations are sufficient to give rise to a steep entropy gradient.

For the locally isothermal simulations, we indeed find that Λ never becomes negative. In the adiabatic case, on the other hand, for $q = 10^{-2}$ (run F), Λ , shown in left panel of Fig. 2, reaches negative values after less than one orbit in the region of the outer spiral wake of the planet, as well as, to a lesser extent, the inner spiral wake. After 100 orbits, zones of buoyant instability are seen throughout the disk, as shown in the right panel of Fig. 2. For the $q = 10^{-3}$ case (run D), Λ achieves negative values for the first ~ 15 orbits, then stays positive for the remainder of the simulation, explaining the relative similarity in resulting surface densities between the corresponding isothermal and adiabatic cases (runs A and D, respectively). These results confirm that buoyant instabilities are consistent with the large-scale disruption of the usual planet-disk interaction features seen in the lower panels of Fig. 1.

3.1.2. Shock heating

In order to determine the role of shock heating in generating the observed buoyant instability, we run another simulation with an adiabatic disk and a $10 M_J$ planet where we exclude heating of the gas due to shocks ($I_{\text{sh}} = 0$; run G). The resulting surface density after 100 orbits, shown in the right panel of Fig. 3, resembles that of the locally isothermal case, where the gap and vortex are visible. This test conclusively shows that the entropy generated in shocks is responsible for the novel phenomena described in the present work.

3.1.3. How strong are the shocks?

In Fig. 4 we show radial profiles of temperature (normalized by the initial temperature profile) and Mach number Ma for 100 orbits in the adiabatic, $10 M_J$ case

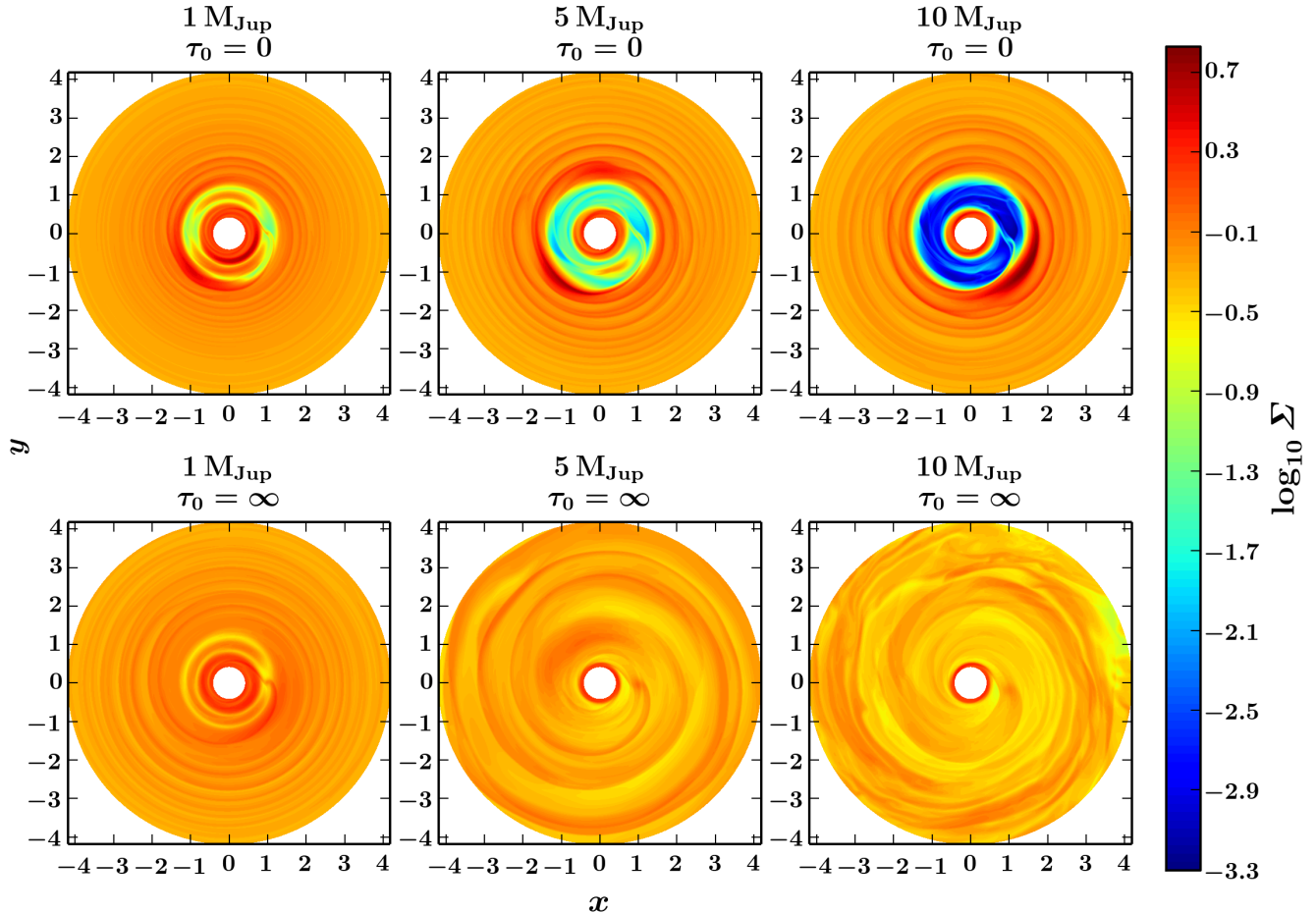


FIG. 1.— Surface densities in the inner disk ($r < 4$) after 100 orbits for locally isothermal ($\tau_0 = 0$) runs A, B, and C, and adiabatic ($\tau_0 = \infty$) runs D, E, and F. Turbulence due to buoyancy appears in adiabatic runs and increases with q (masses based on $M_{\text{star}} \approx 1 M_{\odot}$).

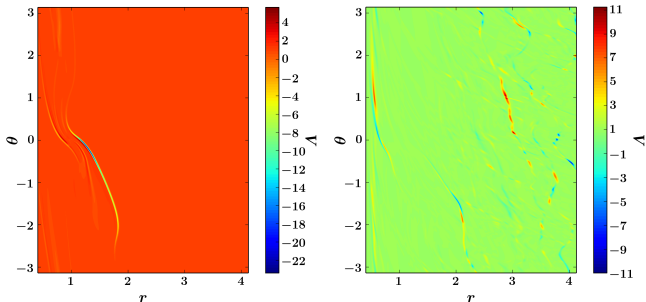


FIG. 2.— Λ for $q = 10^{-2}$ after 1 orbit (left panel) and 100 orbits (right panel) for the inner disk ($r < 4$) in the adiabatic case (run F). Buoyant instability occurs for $\Lambda < 0$. It begins in the outer spiral wake produced by the planet after 1 orbit, while instability is triggered in the inner spiral wake and outer disk soon after.

(run F) at the azimuthal position of the planet. Shocks propagate throughout the disk for the duration of the simulation; however, they do not grow rapidly and monotonically like the temperature, with the strongest shocks ($\text{Ma} > 1.5$) subsiding after ~ 50 orbits. The temperature increases steadily throughout the disk over the course of the simulation. This shows that the temperature increase is not due to a single shock, but due to the

entropy injection of multiple shocks, over the course of many orbits.

3.1.4. Thermal relaxation timescale

To investigate the importance of cooling in non-barotropic disks with high-mass planets, we run several simulations with $q = 10^{-2}$ for cooling times $\tau_0 = 0.1, 1, 10,$ and ∞ orbits (runs H, I, J, and F, respectively). Surface densities after 100 planetary orbits are shown in Fig. 5. Not surprisingly, simulations with shorter relaxation times (0.1 and 1 orbits) more closely resemble the isothermal case: buoyant instabilities and subsequent turbulence are minimal, and so the gap and vortex are preserved. For longer cooling timescales (10 orbits and adiabatic), the shock heating drives buoyant instabilities, generating turbulence that dominates the global structure of the disk, disrupting the gap and vortex.

Because the wake is stationary in the reference frame of the planet, a parcel of gas will be excited by one of the spirals once per synodic period τ_{syn} (with respect to the planet). Therefore, for $\tau_0 < \tau_{\text{syn}}$, the parcel will cool radiatively before encountering the next shock, and thus the energy contributions of successive shocks will not continue to increase the temperature of the parcel beyond that of a single shock. For $\tau_0 > \tau_{\text{syn}}$, however, the

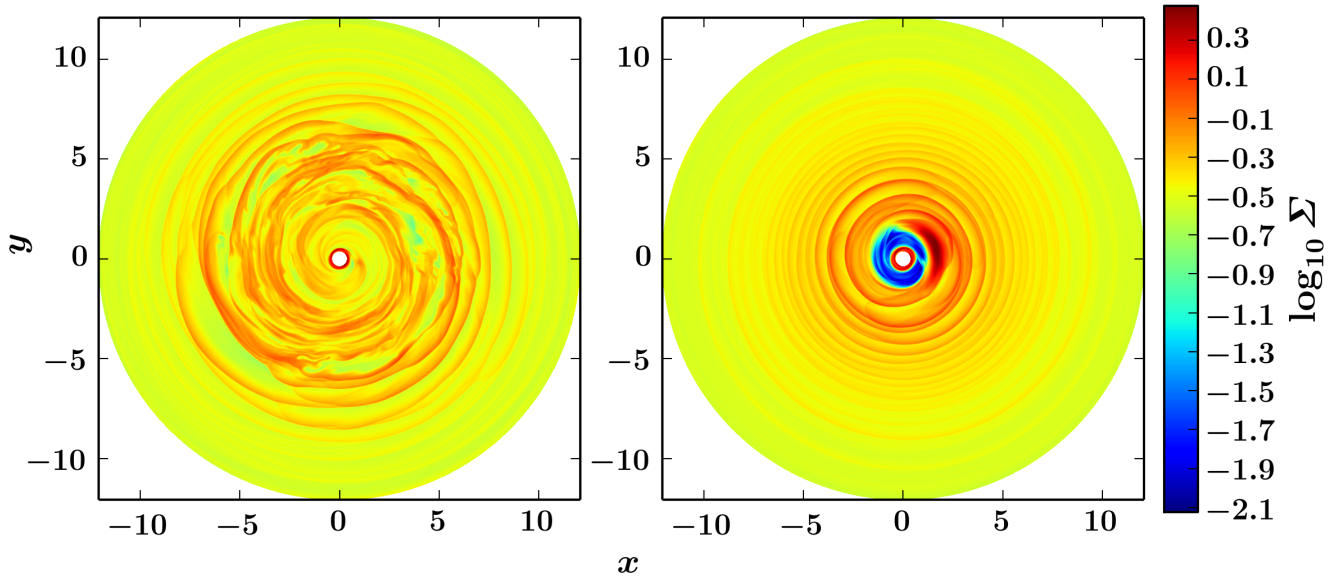


FIG. 3.— Adiabatic simulation of planet-disk interaction of a $10 M_J$ planet (left) with shock heating and (right) without shock heating. This test conclusively shows that the energy dissipated in shocks is driving the instability.

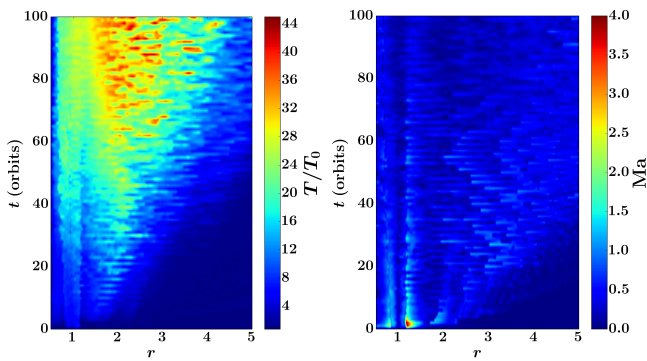


FIG. 4.— Temperature and Mach number for the inner disk ($r < 5$) of run F, at the azimuthal position of the planet. Heating due to shocks initially occurs close to the planet, but spreads to the rest of the disk over the course of the simulation.

gas parcel will not have time to cool to its original temperature before encountering the next shock, therefore the temperature of the gas will continue to rise, even though the energy contributions of each shock will be the same as in the low τ_0 case (since Eq. 10 does not depend on cooling timescale). The emergence of the observed buoyant instabilities therefore depends on the relative orbital and cooling timescale. Its strength depends additionally on the energy contribution of each shock. These are a function of the characteristic differential velocity of the gas flows associated with the spiral wakes, which is in turn determined by the planet’s mass.

3.1.5. Temperature power law

Because the buoyant instability results from the presence of a strong entropy gradient, we compare simulations with differing initial temperature power law slopes β to determine whether a steeper initial entropy gradient enhances the buoyant instabilities generated

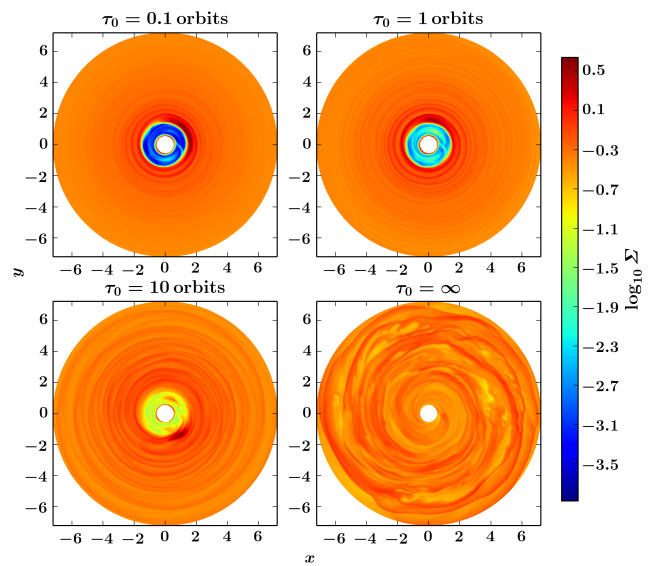


FIG. 5.— Surface densities for the inner half of the disk ($r < 6$) after 100 orbits for four different cooling timescales (runs H, I, J, and F) for a planet with $q = 10^{-2}$.

locally by the planet. We once again use $q = 10^{-2}$ and an adiabatic disk, and conduct runs with $\beta = 0, -0.2, -0.5,$ and -1 , corresponding to runs M, L, K, and F, respectively. The value for run L was chosen to flatten the initial entropy gradient, i.e., $ds/dr = 0$. For $\beta = 0$, Λ is initially positive throughout the disk, while it becomes more negative for decreasing β , so that for these values the disk is initially slightly Solberg-Høiland unstable (see Eq. 16).

The resulting surface densities after 100 planetary orbits for these simulations are shown in Fig. 6. A steep temperature slope (e.g., $\beta = -1$) appears to lead to stronger turbulence, though significant turbulence is

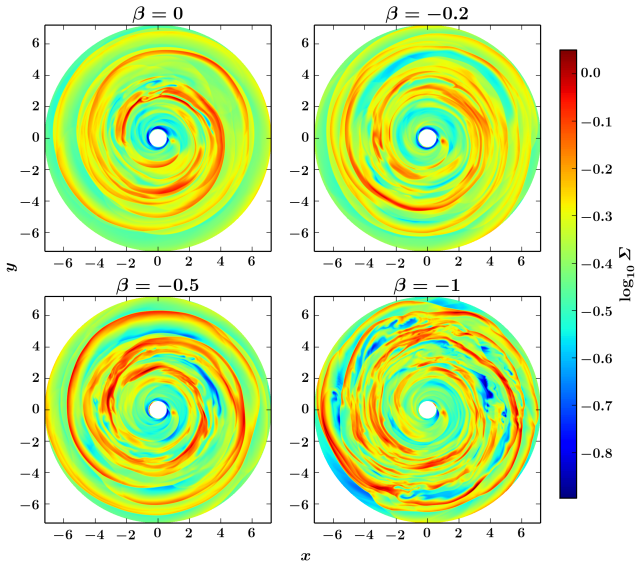


FIG. 6.— Surface densities for the inner half of the disk ($r < 6$) after 100 orbits for four different temperature power law slopes (runs M, L, K, and F). Run M is initially globally stable according to the Solberg-Høiland criterion, but still experiences instability due to heating from the planetary wakes (see Fig. 2).

still observed for $\beta = 0$. The enhancement of the turbulence when the disk is globally unstable supports our hypothesis that the planet generates turbulence by driving local regions into instability, even when the disk is globally stable.

3.2. Angular momentum transport

In order to examine angular momentum transport in the disks simulated in this work and thereby identify possible implications for disk evolution, we calculate effective Shakura & Sunyaev (1973) α -viscosities over time for simulations of locally isothermal and adiabatic disks with $q = 10^{-2}$ (runs C and F). We define an effective viscosity ν in terms of α :

$$\nu = \alpha c_s^2 / \Omega, \quad (17)$$

which drives an accretion rate (assuming a steady state)

$$\begin{aligned} \dot{m} &= -2\pi\nu\Sigma \frac{\partial \ln \Omega}{\partial \ln r}, \\ &= 3\pi\nu\Sigma. \end{aligned} \quad (18)$$

We define also the α value as a function of the kinetic stress $\delta u_r \delta u_\phi$ (where $\delta u_i = u_i - \langle u_i \rangle$, and $\langle X \rangle$ represents the azimuthal average of X)

$$\begin{aligned} \alpha &\equiv \frac{2}{3} \frac{\langle \delta u_r \delta u_\phi \rangle}{\langle c_s^2 \rangle} \\ &= \frac{2}{3} \left(\frac{\langle u_r u_\phi \rangle - \langle u_r \rangle \langle u_\phi \rangle}{\langle c_s^2 \rangle} \right). \end{aligned} \quad (19)$$

Fig. 7 shows α for the aforementioned simulations, calculated once per orbit for 100 orbits.

We find that the evolution of the disk driven by the effective α viscosity differs substantially between the locally isothermal and adiabatic cases. For the isothermal

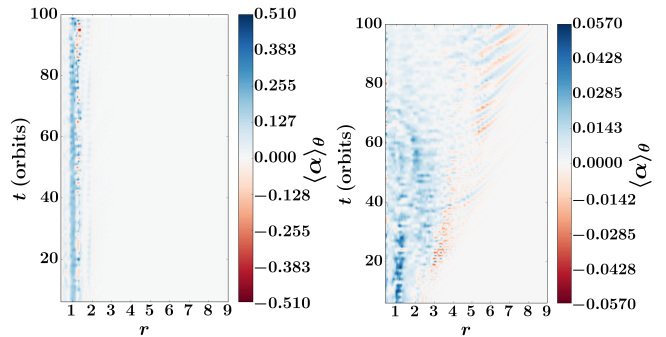


FIG. 7.— Azimuthally-averaged effective α -viscosities for locally isothermal (C; left) and adiabatic (F; right) runs, over the course of 100 planetary orbits, for $r < 9$. The high α values in the isothermal case, taken at face value, imply nearly supersonic turbulence, and indicate that the local α -disk prescription does not properly describe the disk's evolution and that the thin-disk approximation may be breaking down. The thin-disk approximation also limits the adiabatic case: in three dimensions the shocks will be weaker as vertical expansion is allowed. The results nevertheless highlight that shocks in the wakes of high-mass planets are important for mass redistribution.

case (left panel of Fig. 7) the α values are large (reaching 0.5) but occur close to the planet and gap, while the disk beyond $r = 2-3$ remains relatively quiescent. By contrast, the turbulence in the adiabatic case propagates outward through the disk throughout the entire simulation. The α in this case are lower, reaching 0.05, an order of magnitude less. The globally-averaged α between 60–100 orbits is $\approx 0.01-0.02$. The relatively large value of α indicates rapid inward motion of the gas. Defining the accretion timescale

$$\tau_{\text{acc}} \equiv m / \dot{m} \sim \Omega r^2 (c_s^2 \alpha)^{-1}, \quad (20)$$

we find that for a $10 M_{\text{Jup}}$ planet orbiting a $1 M_\odot$ star at 5.2 AU, the characteristic accretion timescale of the disk is on the order of 10^5 years.

We caution that this particular result pertaining to accretion is a function of the cooling time, as for gravitational instability (Durisen et al. 2007; Meru & Bate 2011, 2012), or any shock-driven instability. The high α values in the isothermal case (≈ 0.5) if taken at face value, imply that the rms velocity of the turbulence is approaching supersonic values ($v_{\text{rms}} \sim \sqrt{\alpha} c_s \approx 0.7c_s$). However, this is mainly an indication that the local α -disk prescription does not properly describe the disk's evolution and that the thin-disk approximation may be breaking down. In the adiabatic case, even though the effective α values are reasonably subsonic, the large-scale turbulence is similarly implicated. In three-dimensional runs we expect the shocks to be weaker because of the extra degree of freedom (vertical expansion such as in shock bores; Boley & Durisen 2006) and the efficient radiative cooling of the disk's upper layers, even though the midplane is optically thick and essentially adiabatic.

3.3. BOXZYHYDRO simulations

Müller & Kley (2013) perform 2D simulations of disks containing protoplanets up to $16 M_{\text{Jup}}$ using the FARGO code (Masset 2000; Baruteau 2008), using isothermal and radiative viscous accretion disk models. Their results do not show the strong temperature in-

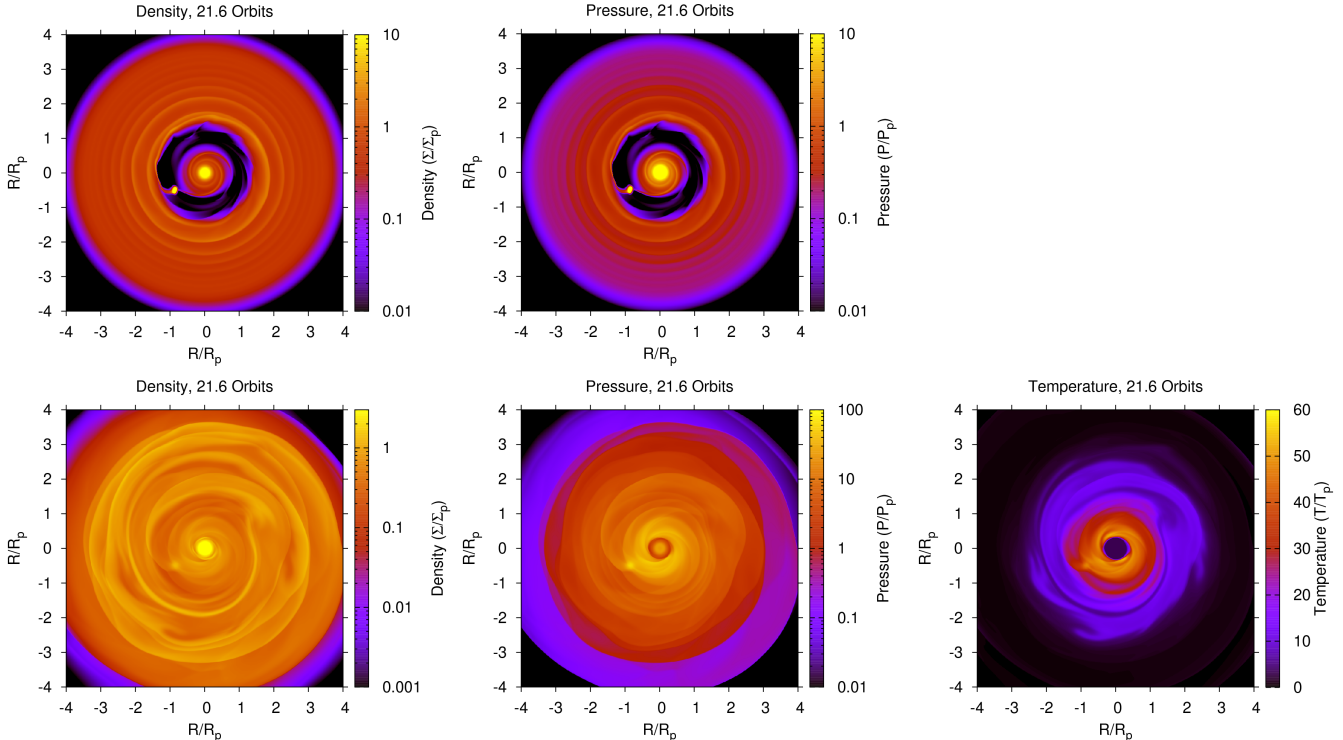


FIG. 8.— BOXZYHYDRO simulations with a $10 M_J$ planet. Surface density, temperature, and pressure are all normalized to the initial values at the planet’s semi-major axis. In the upper panels we show an isothermal control run. A clear spiral structure is seen, along with edge waves by the outer gap wells, evidencing the initial stages of vortex formation. In the lower panels we show an adiabatic run, in which these features are gone. The shock-driven buoyant instability is reproduced with an independent code. BOXZYHYDRO solves for the equations of hydrodynamics in conservative form and uses an approximate Riemann solver for determining fluxes at cell interfaces. It does not require artificial viscosity terms in the energy equation for shock capturing. This rules out the possibility that the instability is effected by Pencil’s numerical shock capturing scheme, evidencing a physical origin for the adiabatic case.

crease seen here. We first suspected that the difference lies in the applied cooling laws: while Müller & Kley (2013) use a cooling function that depends on ρ and T , we apply a fixed, radially dependent cooling. To check this, we performed a calculation defining a dynamical cooling time depending on ρ and T as well. The results were consistent with the fixed, radially dependent cooling time. Unfortunately, Müller & Kley (2013) do not specify whether their code included artificial viscosity in order to properly treat shock heating. If they did, it would enter in their viscous energy dissipation term Q_{visc} , but its form was not specified. A meaningful comparison between our work and theirs is therefore unfeasible.

To resolve this disagreement, and confirm the occurrence of buoyancy-induced turbulence in a 2D, adiabatic disk with a massive protoplanet, we reproduce run F ($10 M_J$, adiabatic) using an independent code, BOXZYHYDRO (Boley et al. 2013). BOXZYHYDRO solves the equations of hydrodynamics in conservative form on a Cartesian grid. An approximate Riemann solver is used, along with standard flux limiting, to describe the fluid states at cell interfaces (e.g., Toro 2009). This allows the code to capture shocks without including explicit artificial viscosity terms in the gas equations.

Using BOXZYHYDRO, we model the disk within the radial range $0.4 < r < 4$ (where the planet’s semi-major axis $r_0 = 1$, as before). The initial setup uses the same

density and temperature profiles, differing only in the details of the boundary conditions and the smoothing of the planet gravitational potential. As the code is Cartesian, there is no strict inner boundary for the grid. The region interior to $r = 0.3$ (≈ 1.6 AU for $r_0 = 5.2$ AU) is locally isothermal to avoid intense heating close to the star. The planet potential is piece-wise smoothed with a cubic spline inside the Hill radius, while keeping the Newtonian profile outside. In comparison, in the Pencil simulations, the Plummer smoothing used there (Eq. (11)) results in a shallower potential well immediately outward of the Hill radius, therefore slightly underestimating the strength of the shocks.

We run the BOXZYHYDRO simulation for 21 orbits. The result is shown in Fig. 8. The upper panels show an isothermal control run, while the lower panels show the adiabatic simulations. The isothermal run shows well-behaved spiral structure, and edge waves in the outer region of the gap, produced by the growing phase of the RWI. In the adiabatic run these features are gone, and instead the code reproduces the main features seen in Pencil’s run F at the same time. At this point, turbulence has already begun to proliferate through the disk, diminishing the gap (which in run F disappears completely at $t \sim 50$ orbits), and suppressing the formation of both inner and outer vortices. These results rule out the possibility that the observed turbulence is an artifact of the shock capturing scheme used in the Pencil Code.

The confirmation by an independent code strengthens the case that the result is not a numerical artifact.

4. DISCUSSION AND CONCLUSIONS

Using 2D, global hydrodynamics simulations of disks with embedded massive planets, we have shown that shocks generated by high-mass planets can significantly raise the temperature of gas in disks. While any given shock is typically weak, with Mach numbers of order unity for $5 M_J$ and up to 4–5 for $10 M_J$, the temperature increase is due to the cumulative effects of shocks, as orbiting gas repeatedly meets the spiral wake (which remains stationary in the reference frame of the planet). If the gas can cool within a synodic period, the energy radiates away between shocks and the situation resembles the isothermal case. If, on the other hand, the cooling time exceeds the synodic period, the mean temperature increases in time. We then see buoyant instabilities driven by both the inner and outer spiral wakes, creating sustained, large-scale turbulence that significantly alters the global structure of the disk.

These results are of particular significance to the frequent interpretation that spiral morphologies are signposts of embedded protoplanets in transition disks. Fits to observed spiral structures are often attempted (e.g., Muto et al. 2012) by making use of linear spiral density wave theory, which depends on the temperature gradient in the disk, as well as the actual disk temperatures (disk aspect ratio). However, because this theory is linear, it relies on assumptions of low planetary mass and local isothermality. In the past few years, some spiral features that have been observed that present problems in interpreting them as having a planetary origin, if linear theory is employed. For example, Juhasz et al. (2014) found that the observed spirals in scattered light would require an increase by a factor of either > 3.5 in surface density or ≈ 0.2 in pressure scale height above the background disk to generate them. They favor the increase in pressure scale height to reproduce the observations. This is consistent with the observed spirals showing in general an opening angle wider than expected from the background temperature. Spiral fitting to the disk MWC 758 (Benisty et al. 2015) at radii $r \approx 80$ – 150 AU needs a large aspect ratio, corresponding to a disk temperature of 300 K at 55 AU, while the surrounding gas is only at ≈ 50 K. Finally, recent observations of HD 100546 (Currie et al. 2014) show a planetary candidate without an associated spiral, and a feature that resembles a spiral arm, but at 90° away from the candidate planet. Moreover, the spiral feature shows little polarization, implying thermal emission at roughly 1000 K. These features are a challenge to linear spiral

density theory but can easily be explained in light of our model, which predicts a significantly different qualitative behavior for spiral structures generated by high-mass planets in radiatively inefficient disks.

In the following paper in this series, we will describe three-dimensional simulations to further explore the role of shock heating from the wakes of massive planets in the structure and evolution of the disk. We caution again that in three dimensions the results will likely differ. Shocks should be weaker for the same planetary mass, given the possibility of vertical expansion. It is possible that the turbulence seen in this work would be seen in another region of parameter space; for instance, it may require a higher protoplanet mass to achieve an effect comparable to that observed in the current work. Moreover, even though the midplane of the disk is optically thick and close to adiabatic, the upper layers might cool efficiently. In this case, the diffusion timescale in the vertical direction may control a given disk’s evolution. We note, however, that the buoyant instability may share similarities to other shock-driven processes, such as gravitational instability (Durisen et al. 2007), where reasonable agreement has been shown between 2D and three-dimensional simulations (see Rice et al. 2014 and references therein). Evidence for similar qualitative behavior is seen in Boley & Durisen (2006), who modeled shocks due to $2.5 M_J$ planets, observing shock bores as gas accelerates upwards and breaking waves as the gas descends back onto the disk, again generating turbulence, though by a different mechanism.

We finally note that heating and buoyancy-induced turbulence may also affect planet migration. Investigating this effect (as in Zhu et al. 2012, but for high-mass protoplanets) would require simulations to be carried out over many more orbits, and for the gravitational back-reaction of the gas on the planet to be included.

AR is funded by NSF AAG grant AST10-09802, and by the Center for Exoplanets and Habitable Worlds (PSU). WL is funded by the National Aeronautics and Space Administration (NASA) through the Sagan Fellowship Program executed by the NASA Exoplanet Science Institute. AB is funded, in part, by the Canada Research Chairs program and The University of British Columbia. M-MML is funded, in part, by NASA OSS grant NNX14AJ56G. This work was performed in part at the Jet Propulsion Laboratory, under contract with the California Institute of Technology (Caltech). The authors acknowledge discussions with Sijme-Jan Paardekooper, Axel Brandenburg, Dhruvadya Mitra, Thayne Currie, and Wilhelm Kley.

REFERENCES

- Avenhaus, H., Quanz, S. P., Schmid, H. M., Meyer, M. R., Garufi, A., Wolf, S., & Dominik, C. 2014, *ApJ*, 781, 87.
 Balbus, S. & Hawley, J. 1991, *ApJ*, 376, 214.
 Baruteau, C. 2008, Ph.D. Thesis, CEA Saclay.
 Benisty, M. et al. 2015, *A&A*, submitted.
 Boley, A. C. & Durisen, R. H. 2006, *ApJ*, 641, 534.
 Boley, A. C., Morris, M. A., Desch, S. J. 2013, *ApJ*, 776, 101.
 Brown, J. M., Blake, G. A., Qi, C., Dullemond, C. P., Wilner, D. J., & Williams, J. P. 2009, *ApJ*, 704, 496.
 Casassus, S., Perez M., S., Jordán, A., Ménard, F., Cuadra, J., Schreiber, M. R., Hales, A. S., & Ercolano, B. 2012, *ApJ*, 754, 31.
 Casassus, S., van der Plas, G., Perez, S., Dent, W.R.F., Fomalont, E., Hagelberg, J., Hales, A., Jordán, A., Mawet, D., Ménard, F., Wootten, A., Wilner, D., Hughes, M., Schreiber, M.R., Girard, J.H., Ercolano, B., Canovas, H., Román, P., & Salinas, V. 2013, *Nature*, 493, 191.
 Currie, Th., Muto, T., Kudo, T. et al. 2014, *ApJ*, 796, 30.
 D’Angelo, G., Durisen, R. H., & Lissauer, J. J. 2011, in *Exoplanets*, ed. S. Seager (Tucson, AZ: University of Arizona Press), 319.
 Durisen, R. H., Boss, A. P., Mayer, L., Nelson, A. F., Quinn, T., & Rice, W. K. M. 2007, in *Protostars and Planets V*, ed. B. Reipurth, D. Jewitt, and K. Keil (University of Arizona Press, Tucson), 951.

- Dzyurkevich, N., Turner, N.J., Henning, Th., & Kley, W. 2013, *ApJ*, 765, 114.
- Flock, M., Ruge, J. P., Dzyurkevich, N., Henning, Th., Klahr, H., & Wolf, S. 2015, *A&A*, 574, 68.
- Garufi, A., Quanz, S. P., Avenhaus, H., Buenzli, E., Dominik, C., Meru, F., Meyer, M. R., Pinilla, P., Schmid, H. M., & Wolf, S. 2013, *A&A*, 560, 105.
- Goldreich, P. & Tremaine, S. 1979, *ApJ*, 233, 857.
- Haugen, N. E. L., Brandenburg, A., & Mee, A. J. 2004, *MNRAS*, 353, 947.
- Hawley, J.F. 1987, *MNRAS*, 225, 677.
- Isella, A., Pérez, L.M., Carpenter, J.M., Ricci, L., Andrews, S., & Rosenfeld, K. 2013, *ApJ*, 775, 30.
- Johansen, A., Youdin, A., & Klahr, H. 2009, *ApJ*, 697, 1269.
- Johansen, A., & Klahr, H. 2005, *ApJ*, 634, 1353.
- Juhász, A., Benisty, M., Pohl, A., Dullemond, C., Dominik, C., & Paardekooper, S.-J. 2014, <http://arxiv.org/abs/1412.3412>
- Klahr, H. 2004, *ApJ*, 606, 1070.
- Klahr, H. & Bodenheimer, P. 2003, *ApJ*, 582, 869.
- Klahr, H. & Kley, W. 2006, *A&A*, 445, 747.
- Kley, W. & Nelson, R. P. 2012, *ARA&A*, 50, 211.
- Kley, W., Müller, T. W. A., Kolb, S. M., Benítez-Llambay, P., & Masset, F. 2012, *A&A*, 546, 99.
- Kunz, M. & Lesur, G. 2013, *MNRAS*, 434, 2295.
- Lesur, G. & Papaloizou, J.C.B. 2010, *A&A*, 513, 60.
- Lin, D.N.C. & Papaloizou, J. 1986a, *ApJ*, 307, 395.
- Lin, D.N.C. & Papaloizou, J. 1986b, *ApJ*, 309, 846.
- Lovelace, R.V.E. & Hohlfield, R.G. 1978, *ApJ*, 221, 51.
- Lovelace, R.V.E., Li, H., Colgate, S.A., & Nelson, A. F. 1999, *ApJ*, 513, 805.
- Lyra, W., Turner, N.J., & McNally, C.P. *A&A*, 574, A10.
- Lyra, W., & Kuchner, M. 2013, *Nature*, 499, 184.
- Lyra, W., & Mac Low, M.-M. 2012, *ApJ*, 756, 62.
- Lyra, W. & Klahr, H. 2011, *A&A*, 527A, 138.
- Lyra, W., Johansen, A., Klahr, H., & Piskunov, N. 2009, *A&A*, 493, 1125.
- Lyra, W., Johansen, A., Klahr, H., & Piskunov, N. 2008, *A&A*, 479, 883.
- van der Marel, N., van Dishoeck, E.-F., Bruderer, S., et al. 2013, *Science*, 340, 1199.
- Masset, F. 2000, *A&AS*, 141, 165.
- Masset, F. & Snellgrove, M. 2001, *MNRAS*, 320L, 55.
- McNally, C. P., Lyra, W., & Passy, J.-C. 2012, *ApJS*, 201, 18.
- Meru, F. & Bate, M. 2012, *MNRAS*, 427, 2022.
- Meru, F. & Bate, M. 2011, *MNRAS*, 411, 1.
- Müller, T. W. A., & Kley, W. 2013, *A&A*, 560, A40.
- Mulders, G. D., Paardekooper, S.-J., Panić, O., et al. 2013, *A&A*, 557, A68.
- Muto, T., Grady, C. A., Hashimoto, J. et al. 2012, *ApJ*, 748, 22.
- Nelson, R.P., Papaloizou, J.C.B., Masset, F., & Kley, W. 2000, *MNRAS*, 318, 18.
- Ogilvie, G.I. & Lubow, S.H. 2002, *MNRAS*, 330, 950
- Oppenheimer, B.R., Brenner, D., Hinkley, S., Zimmerman, N., Sivaramakrishnan, A., Soummer, R., Kuhn, J., Graham, J.R., Perrin, M., Lloyd, J.P., Roberts, L.C., & Harrington, D.M. 2008, *ApJ*, 679, 1574.
- Paardekooper, S.-J. & Mellema, G. 2004, *A&A*, 425L, 9.
- Papaloizou, J. & Lin, D.N.C. 1984, *ApJ*, 285, 818.
- Papaloizou, J.C.B. & Pringle, J.E. 1984, *MNRAS*, 208, 721.
- Papaloizou, J.C.B. & Pringle, J.E. 1985, *MNRAS*, 213, 799.
- Petersen, M. R., Julien, K., & Stewart, G. R. 2007a, *ApJ*, 658, 1236.
- Petersen, M. R., Stewart, G. R., & Julien, K. 2007b, *ApJ*, 658, 1252.
- Quillen, A.C., Blackman, E.G., Frank, A., & Varnière, P. 2004, *ApJ*, 612, 137.
- Raettig, N., Lyra, W., & Klahr, H. 2013, *ApJ*, 765, 115.
- Rafikov, R.R. 2002, *ApJ*, 569, 997.
- Rice, W. K. M., Paardekooper, S.-J., Forgan, D. H., & Armitage, P. J. 2014, *MNRAS*, 438, 1593.
- Shakura, N. I., & Sunyaev, R. A. 1973, *A&A*, 24, 337.
- Shu, F. H. 1992, *The Physics of Astrophysics*, Vol. II (Sausalito, CA: Univ. Science Books).
- Simon, J. B., Beckwith, K., & Armitage, Ph. J. 2012, *MNRAS*, 422, 2685.
- Toomre, A. 1981, What amplifies the spirals. In *The Structure and Evolution of Normal Galaxies*, Proceedings of the Advanced Study Institute, Cambridge, England, Cambridge and New York, Cambridge University Press, 1981, p.111-136.
- de Val-Borro, M., Edgar, R.G., Artymowicz, P., Cieliegl, P., Cresswell, P., D'Angelo, G., Delgado-Donate, E.J., Dirksen, G., Fromang, S., Gawryszczak, A., Klahr, H., Kley, W., Lyra, W., Masset, F., Mellema, G., Nelson, R., Paardekooper, S.-J., Peplinski, A., Pierens, A., Plewa, T., Rice, K., Schäfer, C., & Speith, R. 2006, *MNRAS*, 370, 529.
- Toro, E. 2009, *Riemann Solvers and Numerical Methods for Fluid Dynamics: A Practical Introduction* (Berlin: Springer).
- Varnière, P. & Tagger, M. 2006, *A&A*, 446, 13.
- Wolf, S., Malbet, F., Alexander, R., et al. 2012, *A&A Rev.*, 20, 52.
- Zhu, Zh., Nelson, R.P., Hartmann, L., Espaillat, C., & Calvet, N. 2011, *ApJ*, 729, 47.
- Zhu, Z., Stone, J. M., & Rafikov, R. R. 2012, *ApJ*, 758, L42.